Measurement and prediction of the speed-dependent throughput of a magnetic octupole velocity filter including nonadiabatic effects

Evgueni Nikitin and Elena Dashevskaya
Department of Chemistry, Technion—Israel Institute of Technology, Haifa 32000, Israel

Janis Alnis and Marcis Auzinsh
Department of Physics, University of Latvia, 19 Rainis Boulevard, Riga, LV 1586, Latvia

E. R. I. Abraham, Brendan R. Furneaux, Mark Keil,* Chris McRaven, Neil Shafer-Ray, and Richard Waskowsky†
Department of Physics and Astronomy, The University of Oklahoma, Norman, Oklahoma 73019, USA
(Received 23 August 2002; published 13 August 2003)

A magnetic octupole filter set in a 90° curve produces $\approx 10^8$ cold Rb atoms/s by filtering low-velocity particles from a thermal source. We measure the speed distribution of Rb exiting the filter to be 3.5 K using a Rydberg-atom time-of-flight scheme in which Rb is excited via the process $5s\ ^2S_{1/2} \rightarrow 5p\ ^2P^o_{3/2} \rightarrow 32d\ ^2D$. We develop a general theory of the transmission and speed distribution of particles emitted from such a source including nonadiabatic effects. A detailed Monte Carlo simulation using the theory accurately reproduces the experimental results. We show that for Cs, Li, and Rb atoms and S_2 molecules, nonadiabatic effects do not dramatically effect the performance of the filter, and that the output flux temperatures for a wide variety of filter configurations are well fit to a simple functional form.

DOI: 10.1103/PhysRevA.68.023403 PACS number(s): 39.10.+j, 33.80.Ps, 33.55.Be

I. INTRODUCTION

Ghaffari *et al.* [1] recently reported a ''laser-free'' cold atom source. Their device consists of a Li atomic beam directed into a curved magnetic octupole filter that removes fast-moving particles, transmitting only those moving slowly enough to be guided away from the walls by the octupole field. Though Li can be easily laser cooled, this device offers the simplification of not needing an additional laser [1]. Since it satisfies the primary condition of providing ultracold samples of (magnetic) particles without using laser cooling, it offers an important opportunity to produce a continuous source of cold molecules, for which laser cooling is not amenable. If combined with an optical pumping scheme to continuously load a trap, such as recently demonstrated [2] and proposed [3], the magnetic octupole filter may lead to a dense source of ultracold molecules.

In this work we model and experimentally investigate the characteristics of the magnetic octupole filter. Our goal is to determine properties that will be critical to the use of the device in ultracold atomic and molecular physics, paying close attention to nonadiabatic processes that may limit the output. Specifically, we model the expected transmission and output speed distribution for the alkali-metal atoms ^{6}Li, ^{7}Li, ^{85}Rb, ^{87}Rb, ^{133}Cs and the $K=3$, 9, 15, 21, 27, and 31 rotational states of S_2 over a range of design parameters. We find that the output speed distribution for all of the cases studied may be approximated using a simple effective temperature [Eq. (21)]. In the following section we describe the magnetic octupole filter as implemented in our laboratory. Section III discusses the theory of the motion of particles in the filter, including nonadiabatic effects. Section IV describes a Monte Carlo simulation of the characteristics of the filter. Section V presents the expected transmission and a simple form for the output translational temperature of the device. Section VI describes a Rydberg-atom time-of-flight measurement of the speed distribution of Rb emitted from our filter, and comparisons with our model.

II. DESCRIPTION OF THE OCTUPOLE FILTER

The octupole filter is pictured in Fig. 1. Twelve 3-cm-long octupole filter segments are attached to a liquid-nitrogen reservoir, forming a 90° arc of bend radius $b_r=158$ mm. Each filter segment consists of eight permanent bar magnets of width $a=5$ mm whose alternating north and south poles point toward the center of the filter segment, which is perpendicular to the long axis of each bar magnet. Opposite magnets are separated by a distance, $d=13$ mm. The eight bar magnets are assembled by gluing them onto the faces a plastic octagonal rod and then potting the assembly with vacuum-compatible epoxy. After the epoxy cures, the plastic rod is broken off and the surfaces of the magnets are cleaned.

Our filter is similar to that in Ref. [1], but with several modifications. First, our input is simply a piece of solid Rb that we place about 1 cm outside the first octupole segment, rather than an atomic beam. Another important difference is that our filter magnets can be cooled to 110 K. This effectively eliminates an overwhelming background of room-temperature Rb otherwise emitted by our source. Finally, to provide maximum confinement fields, our NdFeB magnets are contained within the vacuum apparatus.

The magnitude of the magnetic field is zero in the center and approximately 6250 G at the edges, as calculated using

*Present address: Department of Chemical Physics, Weizmann Institute of Science, Rehovot 76100, Israel.

†Present address: Department of Physics, Cameron University, Lawton, OK 73505-6377, USA.

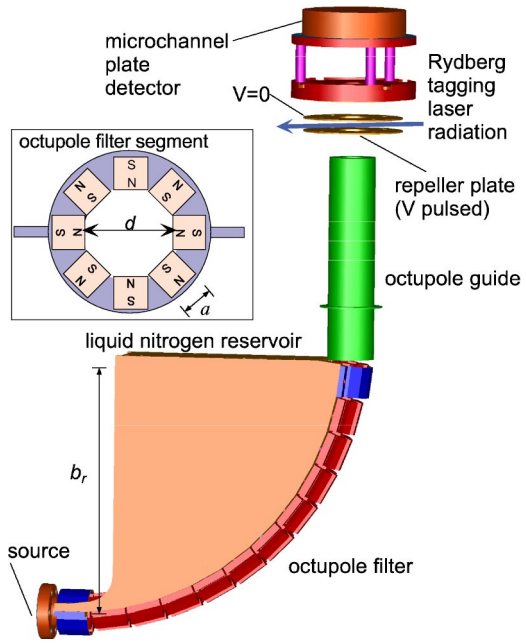

FIG. 1. Experimental apparatus. The slow-moving particles of a vapor emanating from a source placed directly in front of the octupole filter travels through the filter, an octupole guide, and enters a Rydberg-atom time-of-flight detector. To prevent a thermal background of Rb atoms, the filter is cooled with a liquid-nitrogen reservoir.

commercial specifications for the magnetization. Slow-moving, low-field-seeking states of paramagnetic particles are expected to move adiabatically in the filter, reflected by its high-field edges, and therefore always avoiding the cold magnet walls. We calculate the field by assuming an infinite straight guide with the lab-fixed z axis along the guide at the center and ignoring edge effects at the points at which the guide segments come together. Each magnet is described by a magnetization $\vec{M}$ directed radially inward or outward. The z component of the field is zero, and the magnetic field perpendicular to z is calculated directly from the bound surface currents implied by the given $\vec{M}$. The magnitude of the calculated field is shown in Fig. 2. To simplify the calculation of nonadiabatic transitions occurring near the center of the guide, the transverse components of the magnetic field at small r are approximated by

$$(B_x, B_y) = B_0(\cos 3\theta, \sin 3\theta)\left(\frac{r}{a}\right)^3, \tag{1}$$

$$(B_r, B_\theta) = B_0(\cos 2\theta, \sin 2\theta)\left(\frac{r}{a}\right)^3, \tag{2}$$

where x and y, and r and θ are the usual Cartesian and cylindrical coordinates. Here, a is the square dimension of the magnet and $B_o = 0.306\mu_0 M$. The lowest field at the wall occurs at the center of the face of each magnet (given by $3\mu_0 M/2\pi$) and grows much stronger at the edges (Fig. 2). We define the quantity $B_w = (1/2)\mu_0 M$ to be an estimate of the maximum field containing the particles.

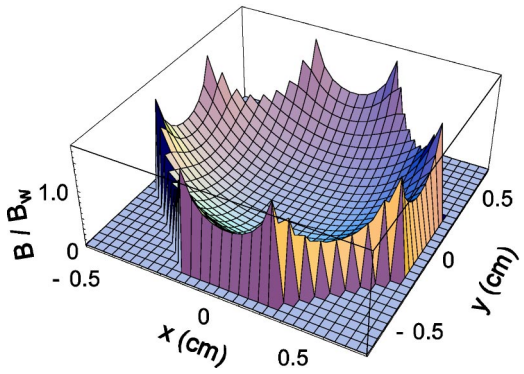

FIG. 2. Two-dimensional cross section of the magnitude of the magnetic field in a section of the guide, where $B_w = \frac{1}{2}\mu_0 M$ is approximately the field at the face of each magnet and M is the magnetization.

III. THEORY OF MOTION OF PARTICLES IN THE FILTER

In this section we develop a general theory of motion for an arbitrary particle with angular momentum $\vec{\mathcal{J}}$ and magnetic moment $\vec{\mu}$ traversing the octupole filter described above. Our model applies to any system with a linear Zeeman splitting at low-magnetic-field strength. The adiabatic motion of a particle in a particular quantum state is determined by the force $\vec{F} = -\vec{\nabla} U$, where U is the Zeeman energy of the particle in that quantum state and is only a function of the magnitude of the magnetic field, $B(\vec{r})$. Of course, only those states whose energy is lowered by decreasing the strength of the magnetic field (low-field-seeking-states) are guided. Particles starting in, and those making transitions into, high-field-seeking states are lost. Once $B(\vec{r})$ and $U(B)$ are determined, $\vec{F} = m\vec{a}$ can be numerically integrated to determine the trajectory. This is sufficient when the field changes slowly compared to the Larmor frequency of the particle. Under these conditions, the magnetic moment $\vec{\mu}$ tracks with the magnetic field, and in the moving frame fixed to the atom, the magnetic field does not change direction. Near the center of the guide where the field goes to zero, this no longer applies, and nonadiabatic transitions to untrapped states can occur.

To consider nonadiabatic motion, we examine the two-dimensional projection of the motion through the field near the center of each octupole, where the magnetic sublevels are close together. In this region, Eqs. (1) and (2) apply, and the Zeeman effect is linear. The forces are small enough that we assume the motion is along straight-line trajectories and the speed is constant. The time-dependent Hamiltonian that describes the evolution of $\vec{\mathcal{J}}$ in the atom-fixed frame running along a classical trajectory is [4]

$$H_{\mathcal{J}} = -\beta g \vec{\mathcal{J}} \cdot \vec{B} - \dot{\vec{\Phi}} \cdot \vec{\mathcal{J}}. \tag{3}$$

Here, the first term is the Zeeman interaction, and the second is the Coriolis interaction that decouples $\vec{\mathcal{J}}$ from $\vec{B}$. The latter is proportional to the angular velocity $\dot{\vec{\Phi}}$ of the rotation of the vector $\vec{B}$ in the atom-fixed frame.

If we assume a straight-line trajectory of a particle traveling at a speed v_0 normal to the z axis, which misses the origin by a distance b and using Eq. (1), the magnitude of the magnetic field and the angular velocity of the field rotation are

$$B(t)=B_0\frac{(b^2+v_0^2t^2)^{3/2}}{a^3}, \tag{4}$$

$$\dot{\Phi}(t)=\frac{3bv_0}{b^2+v_0^2t^2}. \tag{5}$$

When a trajectory traverses the region of nonadiabaticity, the particle undergoes transitions between Zeeman levels. The transition probability $P^{\mathcal{J}}_{mm'}$ from an initial state $\mathcal{J},m$ to a final state $\mathcal{J},m'$ is related to the probability p of an $s=1/2$ to $s'=-1/2$ spin flip of a two-level system by the Majorana formula [5,6]

$$P^{\mathcal{J}}_{mm'}=\frac{\binom{2\mathcal{J}-m-m'}{\mathcal{J}-m}\binom{4\mathcal{J}}{2\mathcal{J}}}{\binom{2\mathcal{J}+m+m'}{\mathcal{J}+m}\binom{4\mathcal{J}}{2\mathcal{J}+m+m'}}p^{2\mathcal{J}} \tag{6}$$

$$\times\left[\sum_r\binom{\mathcal{J}-m}{r}\binom{\mathcal{J}-m'}{r}\times\left(\frac{1-p}{p}\right)^{[(m+m')/2]+r}(-1)^rS_r\right]^2, \tag{7}$$

$$S_r=\begin{cases}\dfrac{\binom{2\mathcal{J}}{2\mathcal{J}-m-m'}}{\binom{m+m'+r}{r}} & m+m'>0\\[2ex] \dfrac{\binom{r}{r+m+m'}}{\binom{2\mathcal{J}-m-m'}{2\mathcal{J}}} & m+m'<0.\end{cases} \tag{8}$$

Here we have rewritten the Majorana formula in terms of binomials for computational purposes.

The quantity p can be calculated from the solution of the time-dependent two-state problem of spin reversal. This problem is formulated in terms of two coupled equations for the probability amplitudes $a_{\pm 1/2}$ for being in the $s=1/2$ and $s=-1/2$ states:

$$\dot{a}_{1/2}=\dot{\Phi}\exp\left(-i\int_0^t\omega(t)dt\right)a_{-1/2}, \tag{9}$$

$$\dot{a}_{-1/2}=-\dot{\Phi}\exp\left(i\int_0^t\omega(t)dt\right)a_{1/2}, \tag{10}$$

where $\omega(t)$ is the Zeeman energy in angular frequency units. Using Eqs. (4) and (5) and introducing the dimensionless time $\tau=v_0t/b$, we can rewrite Eqs. (9) and (10) as

$$\frac{d^2a_{1/2}}{d\tau^2}+\left(i\xi(1+\tau^2)^{3/2}+\frac{2\tau}{1+\tau^2}\right)\frac{da_{1/2}}{d\tau}+\frac{9}{4(1+\tau^2)}a_{1/2}=0, \tag{11}$$

where

$$\xi=\frac{\mu_Bg B_0b^4}{2\hbar a^3v_0} \tag{12}$$

is the dimensionless Massey parameter. Given a straight-line trajectory, we numerically integrate Eq. 11 to the limits as $\tau\rightarrow-\infty$ and $+\infty$. Without integrating to these limits, the calculation is unstable and unreliable. If we assume that at $\tau=-\infty$, $a_{1/2}=1$ and $\dot{a}_{1/2}=0$, the transition probability is $p=1-\lim_{\tau\rightarrow\infty}|a_{1/2}|^2$. We fit an equation of the form:

$$p=e^{-(\pi\xi)^{1/2}}\cos^2(2.1\xi^{1/4}+0.54\xi^{1/2}) \tag{13}$$

to numerical solutions of Eq. (11) for several values of ξ. The agreement between Eq. (13) and the numerical solutions of Eq. (11) is sufficient to use Eq. (13) in the subsequent calculations.

For the case that ξ is large, the probability of transition p is small and $P^{\mathcal{J}}_{mm'}\rightarrow\delta_{mm'}$. This corresponds to the case where the Larmor frequency is large compared to the rate of change of the magnetic-field, and the magnetic field projection is preserved absolutely. For the case that $\xi=0$, $p=1$ and $P^{\mathcal{J}}_{mm'}=\delta_{m,-m'}$. This corresponds to the case where the magnetic field changes 180° instantly. The magnitude of the projection of $\vec{\mathcal{J}}$ is preserved, but it now lies in the opposite direction relative to $\vec{B}$. For intermediate values of ξ and p, all elements of $P^{\mathcal{J}}_{mm'}$ are nonzero.

IV. NUMERICAL SIMULATION OF TRAJECTORIES

We use the general formalism described above to numerically simulate the trajectories of ^{6}Li, ^{7}Li, ^{85}Rb, ^{87}Rb, ^{133}Cs and the $K=3$, 9, 15, 21, 27, and 31 rotational states of diatomic sulfur, whose ground electronic state is $^3\Sigma_u^-$, an example of a typical Hund's case (b) molecule with an appreciable magnetic moment. For most of the simulations presented here, the initial location of the particle is chosen randomly from a source consisting of a flat plate with a diameter that matches the inner diameter of the filter and is placed directly in front of the first filter segment. As will be seen in Sec. VI, the final speed distribution is sensitive to the size and placement of the source. The speed of the particle is taken randomly from a Maxwell-Boltzmann speed distribution of temperature T_{source}, and the direction of the velocity is chosen at random within the hemisphere above the plate source. The source temperature T_{source} is taken to be 300 K for each simulation, except where otherwise stated.

For the case of the alkali-metal atoms, $\mathcal{J}$, m, and g from the general formalism are replaced by F, m_F, and g_F. At the low fields near the center of the filter, $U(B)=m_F g_F \mu_B B$. At the high fields near the walls of the tube, the electronic spin decouples from the spin of the nucleus. While the output of the different alkali-metal atoms is expected to be similar, because two mass scales exist at high and low magnetic-field strengths, we simulate several alkali-metal atoms for completeness. Thus, we use the Breit-Rabi formula for U [7], valid at all fields occurring in the filter.

The $^3\Sigma_u^-$ ground state of S_2 is described by the nuclear rotation quantum number K, electronic spin S, total angular momentum (excluding nuclear spin) J, and magnetic quantum number m_J. The field-free energy levels are given by

$$E(K,J)=\begin{cases} B_{rot}K(K+1)-\lambda-f_\lambda[2K-1]-\gamma K, & J=K-1 \\ B_{rot}K(K+1), & J=K \\ B_{rot}K(K+1)-\lambda+f_\lambda[2K+3]+\gamma(K+1), & J=K+1, \end{cases} \tag{14}$$

$$f_\lambda[\alpha]=\alpha B_{rot}-\sqrt{\alpha^2 B_{rot}^2+\lambda^2-2\lambda B_{rot}}. \tag{15}$$

For S_2, the spectroscopic constants are $B_{rot}=0.3\ \mathrm{cm}^{-1}$, $\lambda=12\ \mathrm{cm}^{-1}$, and $\gamma=-0.006\ \mathrm{cm}^{-1}$ [8]. Nuclear-spin statistics dictates that K is odd. The large value of λ leads to splittings of rotational levels by several wavenumbers. This is in contrast to the hyperfine states of the alkali-metal atoms that are split typically by a few tenths of a wave number. This order-of-magnitude increase in interaction strength causes the electronic spin to be strongly coupled to the nuclear axis at all points throughout the filter. It is therefore reasonable to use a Hund's case (b) coupling scheme throughout, and assume that the linear Zeeman effect applies at all points in the filter. The Zeeman energies are [9]

$$U_{K,J}=m_J g_{JK}\mu_B B, \tag{16}$$

where

$$g_J=\begin{cases} \dfrac{-g_e}{J+1}, & J=K-1 \\ \dfrac{g_e}{J(J+1)}, & J=K \\ \dfrac{g_e}{J}, & J=K+1. \end{cases} \tag{17}$$

Because the potential scales as $1/J$ for $J=K\pm1$, but as $1/J^2$ for $J=K$, far less of the $J=K$ component of the K-state triplet will move through the filter. This suppressed Zeeman effect is due to the fact that since $\vec{J}=\vec{K}+\vec{S}$, if $J=K$, then $\vec{S}$ is roughly perpendicular to $\vec{J}$. The nuclear rotation therefore averages the projection of $\vec{S}$ on $\vec{J}$ to be nearly zero, causing the interaction of the electronic spin with the magnetic field to be very small. Since the magnetic g factor of all molecular states is inversely related to J, we expect to guide only molecules in the lowest rotational levels.

After determining the initial velocity of a particle, we randomly choose an initial quantum state and integrate Newton's equations of motion using the potentials described above. Since U is only a function of the magnitude of the magnetic field $B(\vec{r})$, and derivatives of B^2 are more easily computed, we rewrite the force as

$$\vec{F}=-\frac{\partial U(B)}{\partial B}\frac{\vec{\nabla}B^2}{2B}. \tag{18}$$

An analytical form for the field valid everywhere in the filter is found and differentiated. A bicubic spline to B^2 and $\partial_x B^2$ and $\partial_y B^2$ is carried out to allow for rapid evaluation of the force to an accuracy of at least one part in 10^3. A variable time step is used to ensure that the position of the particle does not change by more than 1% of the inner diameter of the tube, and the kinetic energy of the particle does not change by more than 2% during each such integration step. At each integration step the speed of the particle is adjusted to ensure a constant total energy.

We allow for the possibility that m can change each time the distance between the particle and the center line of the filter becomes a minimum. We calculate the Massey parameter ξ from Eq. (12) for this crossing event, where v_0 is the speed of the particle at the minimum distance b from the center. After determining ξ, the probability that a spin-(1/2) particle changes state, p is determined from Eq. (13), and the Majorana formula is used to find the probability that an $m \rightarrow m'$ transition occurred. By evaluating binomials rather than factorials in the Majorana formula, the expression is stable for $J\leqslant 34$ for S_2. After evaluating $P^J_{mm'}$, a new value of m is randomly chosen from this weighted distribution. If an m changing event occurs, the total potential energy is adjusted to accommodate the change in Zeeman energy without changing the speed of the particle. In the region where nonadiabatic transitions occur, the energy difference between any two Zeeman levels is much lower than the kinetic energy.

Trajectories are carried out until the particle hits the wall of the filter or exits the guide. The transmission T is then taken to be the fraction of trajectories that exit the guide, multiplied by the fraction of the initial velocity distribution sampled. For the case of alkali-metal atoms, kT_{source} is large compared to the hyperfine splitting, so we assume equal distribution of Zeeman sublevels. Only those that start in the

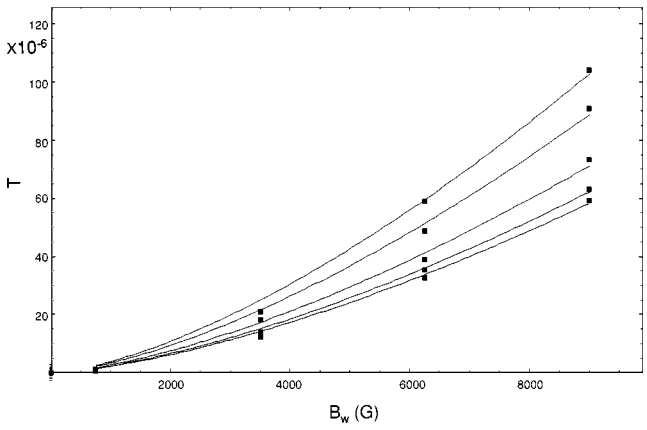

FIG. 3. Simulated transmission of ^{85}Rb as a function of field strength B_w and $\gamma = d/b_r$, where d is the inner diameter and b_r is the bend radius of the filter. From the upper to the lower curve, the plots correspond respectively to γ of 0.04, 0.2, 0.12, 0.2, and 0.28. The points are the result of the Monte Carlo simulation, whereas the smooth lines are a fit to the points by the function $T = \text{const}(B_w^{3/2})$.

upper hyperfine state $F = I + S$ will be guided. We allow the possibility of being in any Zeeman level of the upper hyperfine state (the $m_F = -F$ state may make a nonadiabatic transition into a trapped state before it is lost) and weight all our final distributions by a fraction $(2I+2)/(4I+2)$ to account for those initially in the lower hyperfine state that were lost. For the case of S_2, kT_{source} is comparable to the rotational splitting. The transmission of each state is *not* weighted by its thermal population, but each rotational level is simulated separately. The reported transmission will be the fraction of particles relative to the number originally present in the given rotational level.

V. RESULTS OF THE NUMERICAL SIMULATION

We expect the output to depend on the magnetic field B_w, the source temperature T_{source}, the bend radius b_r, the inner diameter d, and particle species. The fraction of trajectories that travel through the filter without hitting its walls obviously increases as the magnetic field strength increases. Provided the source temperature is greater than the final temperature so that the speed distribution grows as v^2 for the range of speeds transmitted by the filter, T_{source} does not effect the output speed distribution and the transmission fraction scales simply as $T_{\text{source}}^{-3/2}$. (For this reason, except where otherwise stated, T_{source} is taken to be 300 K.) We study the effect of changing geometry in terms of the ratio $\gamma = d/b_r$. If one assumes a simplified potential that is zero in the center, and a step function to a maximum energy at the walls of the filter, then the transmission will be dependent only on the ratio γ. As the device becomes smaller, the increased acceleration needed to keep a particle in the circular orbit is provided by an increased frequency of collisions with the walls. We also expect the transmission for the more realistic adiabatic force field [Eq. (18)] to be relatively insensitive to the physical size of the filter. Throughout this discussion we fix the bend radius to that of our apparatus ($b_r = 158$ mm). For

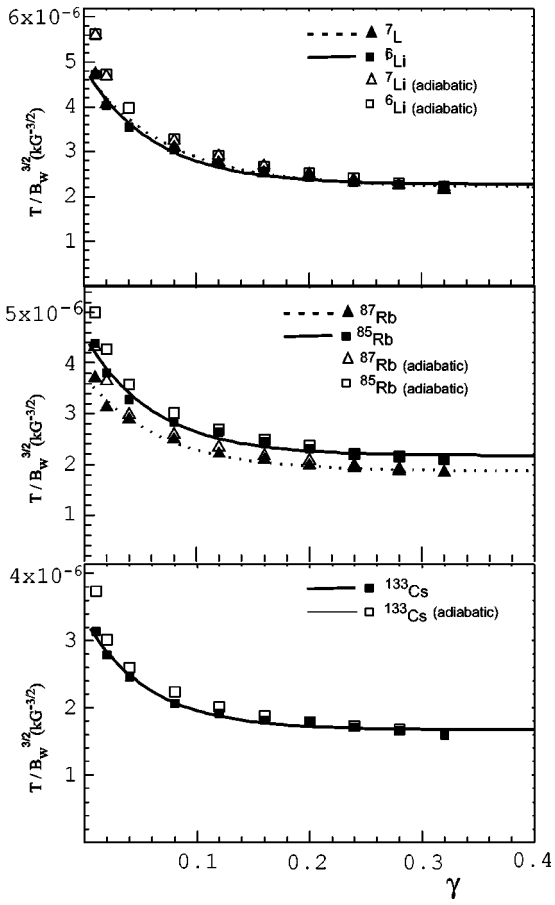

FIG. 4. Transmission of Li, Rb, and Cs atoms divided by $B_w^{3/2}$. Solid squares and triangles are the simulated transmission. Heavy solid and dotted lines are fits of the simulated transmission to guide the eye. Unfilled squares and triangles are simulated transmissions assuming only adiabatic motion.

computational purposes, the 300 K speed distribution of the source is truncated so that hopelessly fast particles are not considered, and the velocity direction is limited to a divergence of 35° for $\gamma = 0.01$ to 85° for $\gamma = 0.32$. We include any particles that start outside these limits as lost in the final transmission, and we verified numerically that an insignificant number of such particles exit the filter.

The transmission fraction coefficient T as a function of field strength B_w and bend ratio γ for the case of ^{85}Rb is given in Fig. 3. We find that the numerical results for T are fit reasonably well (to 10% accuracy) by a $B_w^{3/2}$ power law. This power law is exactly what is expected from a device that simply filters out all particles moving with energy greater than a cutoff energy proportional to B_w. Figure 4 gives the transmission multiplied by $B_w^{3/2}$ for ^{85}Rb, ^{87}Rb, ^{6}Li, ^{7}Li, and ^{133}Cs. The transmission of the different atoms varies by 20%. As the geometry of the filter changes from $\gamma = 0.32$ to $\gamma = 0.01$, there is a slight increase in the transmission fraction. A more narrow filter allows faster particles to pass due to more grazing incidence collisions with the walls. The input flux into the filter is expected to fall as the area of the entrance to the filter, which is proportional to γ^2. The fact that the transmission fraction is only slightly stronger for

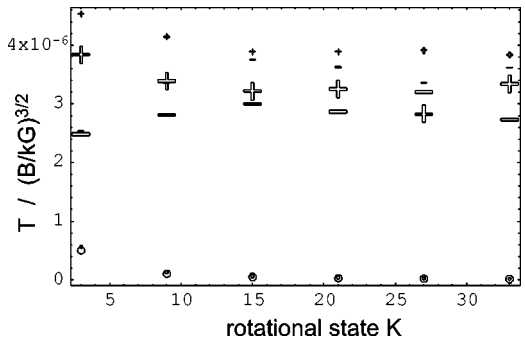

FIG. 5. State-dependent transmission T for S_2 divided by $B_w^{3/2}$ for $\gamma=0.08$. (γ is the ratio of inner diameter of the filter to bend radius.) Plus signs indicate $J=K+1$; circles, $J=K$; and minus signs, $J=K-1$. Large symbols indicate the calculated transmission whereas small symbols indicate the calculated transmission ignoring nonadiabatic effects.

small values of γ implies that slow molecule production will be greater for a filter of large inner diameter. We conclude that the probability of an alkali-metal atom passing through the filter is approximately $T\simeq 10^{-6}\,(B_w/\mathrm{kG})^{3/2}$. Also shown in Fig. 4 is the simulated transmission when complete adiabatic motion is assumed. We see that such an assumption overestimates the transmission by a factor of 20% for a narrow filter with $\gamma=0.01$. The reduction in throughput due to nonadiabatic motion becomes insignificant as γ increases and the frequency of passing through the zero-field region decreases.

Figure 5 gives the simulated value of $T/B_w^{3/2}$ for S_2 as a function of J and K for $\gamma=0.08$ (the ratio for the current apparatus). Notice that very little of the $J=K$ states is transmitted compared to the $J=K\pm1$ states, as expected from the weak interaction of the $J=K$ states with the magnetic field. Notice also that the effect of nonadiabatic m_J-changing transitions is more dramatic for S_2. For the alkali-metal atoms in the upper hyperfine state, nonadiabatic motion will lead to loss only when $m_F'=-F$. All the other m_F' states are still low-field seeking in the high-field limit. For the case of S_2, all final states for which $m_J' g_{JK}<0$ will be lost. It is this larger fraction of high-field-seeking final states that causes a more substantial loss due to nonadiabatic transitions. For example, for $\gamma=0.08$, the transmission of the $K=3$, $J=4$ state of S_2 is decreased by 12%. Finally, we note that as a function of magnetic field (750 G$<B_w<$9000 G for the alkali-metal atoms and 750 G$<B_w<$6250 G for S_2) we find that the numerical results for T are still fit to 10% accuracy by the $B_w^{3/2}$ power law.

To study the possible speed distributions of particles exiting the filter, we consider 226 different cases, specifically, for the atoms ^{6}Li, ^{7}Li, ^{85}Rb, ^{87}Rb, and ^{133}Cs, for field strengths $B_w=750$, 3500, 6025, and 9000 G, for $\gamma=d/b_r=0.01, 0.02, 0.04, 0.08, 0.12, 0.16, 0.20, 0.24, 0.28$, and 0.32. In addition to the alkali-metal atoms we examine the $K=3, 9, 15, 21, 27$, and 31 rotational states of S_2 for $\gamma=0.08$ and $B_w=6250$ G. Figure 6 shows the predicted speed distribution of ^{85}Rb as a function of B_w and γ. In agreement with the previous analysis of the transmission fraction, the

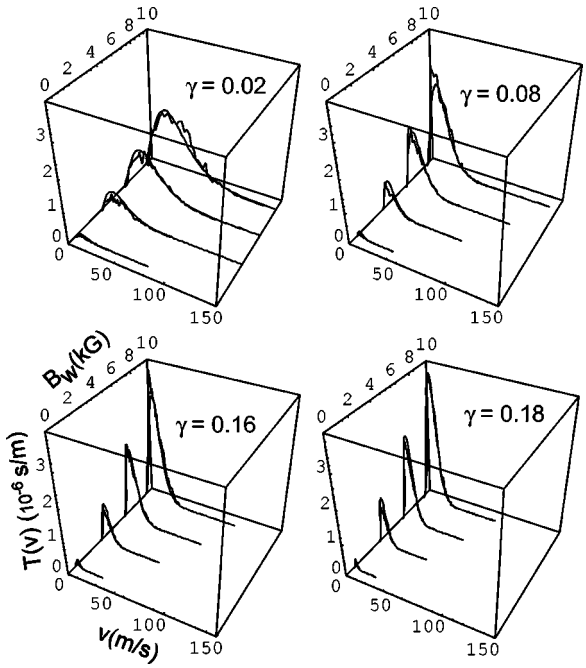

FIG. 6. Speed-dependent transmission $T(v)$ of ^{85}Rb for various magnetic fields and values of γ (the ratio of inner diameter of the filter to bend radius).

speed distribution gets cooler as the magnetic field decreases or γ increases. We define v_c as the cutoff velocity: the maximum velocity of a particle leaving the source (in a direction normal to the source plate) such that the collision energy with the wall is less than the confining potential at a magnetic field B_w,

$$v_c=\sqrt{\frac{2\mu_c B_w}{m}}\frac{2+\gamma}{(4\gamma+\gamma^2)^{1/2}}, \tag{19}$$

where

$$\mu_c=\begin{cases}\dfrac{1}{2}g_F\mu_B & \text{for alkali-metal atoms,}\\ Jg_{JK}\mu_B & \text{for } S_2.\end{cases} \tag{20}$$

When scaled to this velocity, the final speed distribution $P(v/v_c)$ is nearly independent of initial quantum state and magnetic field strength. Figure 7 shows the overlay of these distributions as a function of v/v_c. Remarkably, all distributions with $\gamma>0.02$ are reasonably fit to a Maxwell-Boltzmann speed distribution for the temperature

$$T_{\mathrm{eff}}=\frac{(2+\gamma)^2\mu_c B_w}{3.5(4\gamma+\gamma^2)k_B}. \tag{21}$$

However, for $\gamma\leqslant0.02$, the scaled distributions are colder than predicted by T_{eff}. Thus, for design purposes for many applications, the temperature of the output flux can be estimated with this simple formula.

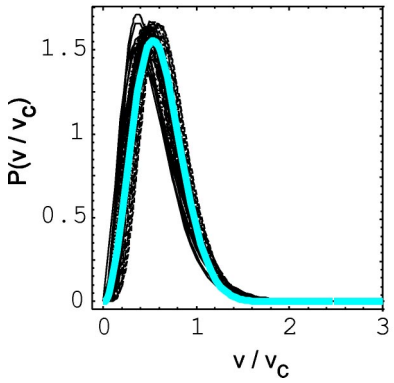

FIG. 7. Dark lines are the scaled speed-dependent transmission $T(v)$ of ^{85}Rb, ^{87}Rb, ^{6}Li, ^{7}Li, ^{133}Cs, and S_2 with $K=3,9,15,21,27,33$ at bend ratios ranging from $\gamma=0.02$ to $\gamma=0.32$, and fields ranging from $B_w=750$ G to $B_w=9000$ G. The light line is the Maxwell-Boltzmann speed distribution at the temperature T_{eff} given by Eq. (21).

VI. EXPERIMENTAL RESULTS

A glass vial containing Rb is placed in a thin-walled stainless steel tube that is attached just outside the guide. The tube is crushed with a pair of pliers, creating a source of Rb that sits just outside the bottom of the first octupole segment. Our numerical simulations of the output speed distribution can quantitatively distinguish between initial conditions at this level.

We probe the speed distribution of Rb emitted from our filter using the method of Rydberg-atom time-of-flight spectroscopy [10]. We probe Rb atoms located in an extraction region between two plates separated by 8.84 mm (Fig. 1). The Rb atoms are first excited to the $5p\,^2P_{3/2}$ state using $\lambda_{\text{vac}}=780.241$ nm laser radiation. This radiation is produced from a Lambda Physik Scanmate IIe dye laser pumped by a nanosecond pulsed Nd:YAG (where YAG stands for yttrium aluminum garnet) laser (Modified Spectra Physics DCR laser, Larry Wolford Services). The $\lambda_{\text{vac}}=481.754$ nm output of a second pulsed dye laser (Spectra Physics PDL II pumped by a Continuum Shurlite) irradiates the Rb in coincidence with the 780.241 nm laser radiation, exciting the Rb from the $5p\,^2P_{3/2}$ to the $32d\,^2D$ state. The 780.241-nm and 481.754-nm beams have a repetition rate of 10 Hz and cylindrically focused in a plane perpendicular to the time-of-flight axis to 1.9 mm and 0.80 mm, respectively, as measured by the razor blade method.

In addition to the successful $5s\rightarrow5p\rightarrow32d$ probe scheme, several unsuccessful schemes were carried out: Direct ionization by 212.8-nm light led to a flood of background ions. Ionization using 322.893-nm light to excite the $9p$ state of Rb followed by photoionization with 1064-nm laser radiation did not lead to a background ion problem. However, because ions were created instead of neutral Rydberg atoms, stray electric fields during the drift time caused the probe to be insensitive to speeds on the order of 10 m/s. Direct excitation to the p Rydberg series using 296-nm laser radiation served well to measure the speed distribution of Rb from a simple room-temperature source, but the UV laser radiation produced too many background ions to measure the output of the filter accurately.

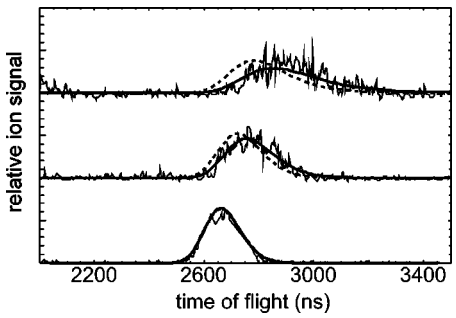

FIG. 8. Comparison of the measured time-of-flight distribution of Rb (thin line) to the expected distribution (thick line). The dashed line gives the expected speed distribution from a uniform source. The three sets of curves represent three different delay times τ between the Rydberg-tagging laser and the ionization pulse: the lower set corresponds to $\tau=0$ μs, the middle set corresponds to $\tau=15$ μs, and the upper set corresponds to $\tau=31$ μs.

After waiting for a delay time of 0–31 μs, the excited $32d\,^2D$ Rb is field ionized by a 460 V pulse applied to one of the extraction plates. This pulse creates a 525 V/cm field which is maintained long enough to force the Rb^+ ions into a field-free time-of-flight region that is 50.8 mm in length. After traveling through this region, the ions strike a flat microchannel plate detector with a 25 cm^2 active area. The signal current due to Rb^+ ions is then recorded with a digital computer. The time-of-flight for delay times between 0 and 31 μs are shown in Fig. 8. Under these conditions, the spread in arrival time of the ions is determined by the spatial distribution at the time of the extraction pulse. When the delay between laser excitation and pulsed field extraction is 31 μs, Rb with a speed of 33 m/s moves closer to the detector by 1 mm, corresponding to the width of the cylindrical focus. The fact that the pulse drifts by roughly the original full width at half maximum of the 0 μs delay pulse in 31 μs suggests that the mean velocity of the beam is close to that predicted by our model. To compare the observed time-of-flight spectrum to the predicted speed distributions of Fig. 8, we run a Monte Carlo simulation of the time-of-flight apparatus. We treat the position of the cylindrical focus as well as the beam width as adjustable parameters in order to obtain the best fit to the zero-time-delay spectra. The beam width determined in this manner is 0.68 mm, which is in reasonable agreement with the measured value of 0.80 mm.

Simulated time-of-flight spectra for the speed distribution resulting from the model (dotted line) are compared to the data in Fig. 8. We believe the discrepancy is due to the model of the Rb source. For all calculations presented in the preceding section, the size of the source is assumed to be equal to the inner diameter of the filter. We now consider a system that more closely matches the experimental conditions. We assume a 1-mm-diameter source placed at the outside edge of the octupole filter. In this case we expect more fast moving trajectories that graze the outside edge to make it through the filter. Thus we expect the small source to lead to a warmer distribution than the large source. The simulated speed distribution in this case is given as the solid line in Fig.

8. Thus the observed time-of-flight spectra is consistent with the Rb at the source of our filter being concentrated at the bottom of the first octupole segment. However, we cannot completely rule out the possibility that the distribution is hotter than expected from a uniform source because of collisions that preferentially knock away slow moving particles.

Numerical simulation of the experimental conditions indicates a transmission $T=1.6\times10^{-5}$. The rate with which particles leave the filter is simply the rate with which particles enter the filter multiplied by this transmission. To determine the input flux, the temperature of the Rb source, the placement of the source with respect to the entrance of the first octupole segment, the steering of cold particles away from the source by fringe fields, and the number of collisions experienced by cold particles entering the filter, must be known. While these factors are difficult to know accurately, the strength of the ion signal observed provides an experimental estimate of the flux. By comparing the integrated time-of-flight spectra at short time delays to that of a single ion, we conclude that we observe approximately 80 Rb ions per laser shot. A study of the Rb signal as a function of laser power indicates that both the $5s\,^2S_{1/2}\rightarrow5p\,^2P^o_{3/2}$ and $5p\,^2P^o_{3/2}\rightarrow32d\,^2D$ transitions are saturated, implying that the Rydberg state is populated with an efficiency of $\approx25\%$. By taking account of the ion optics and the quantum efficiency of the microchannel plate (MCP) detector, we estimate that $\approx50\%$ of the Rb initially populated in a Rydberg state is detected. From these considerations we estimate that $N\approx640$ particles are in the volume of the laser radiation during each laser shot. The probe laser is a distance of $d_{\rm laser}=20$ mm from the exit of the octupole filter, and unfocused, fills a volume of $V_{\rm laser}=400$ mm^3 in front of the 2.54-cm-wide MCP detector. Assuming the particles exit the guide uniformly in a hemisphere, the fraction of particles entering the laser volume is $A/2\pi d^2_{\rm laser}$, where A is the perpendicular cross-sectional area of the laser. The number of particles in the laser volume per laser shot is then given by the fraction entering times the transit time across the laser beam, $w/\bar{v}$, where w is the transverse beam waist and $\bar{v}=27$ m/s is the average output speed of particles exiting the filter, as determined from the simulations. The rate of Rb leaving the filter is thus related to N by

$$R_{\rm filter}=\left(\frac{V_{\rm laser}}{2\pi d^2_{\rm laser}}\frac{1}{\bar{v}}\right)^{-1}N\approx10^8 \text{ particles per second.} \tag{22}$$

VII. SUMMARY

We have investigated the properties of an octupole filter for the production of cold atoms and molecules. We have found that the speed distribution of particles leaving the filter is approximated by a Maxwell-Boltzmann distribution of temperature $T_{\rm eff}$ that has a simple functional form [Eq. (21)]. The apparatus we constructed is predicted to produce a beam of Rb at $T_{\rm eff}=1.5$ K. We developed a sensitive probe of slow-moving Rb atoms and observe a Rydberg-atom time-of-flight spectrum corresponding to a temperature of $T_{\rm exp}=3.5$ K. This difference in temperature is shown to be consistent with the uncertainty in the geometry of the Rb source at the entrance to the filter. We predict that the transmission for the S_2 molecule and a variety of alkali-metal atoms is a few parts per million. We developed a formalism for predicting the effect of nonadiabatic motion. While nonadiabatic motion is not overly important in the current experiment, it plays an increasingly significant role for smaller filter diameters and is likely more of a problem for molecules than for alkali-metal atoms. Finally, we observe a flux of ^{85}Rb through our filter of about 10^8 atoms s^{-1}.

ACKNOWLEDGMENTS

This work was supported by the U.S. Office of Naval Research (Grant No. N00014-01-1-0668), the National Science Foundation (Grant No. CHE-9875456), and The University of Oklahoma Vice President for Research.

[1] B. Ghaffari *et al.*, Phys. Rev. A **60**, 3878 (1999).
[2] J. Stuhler *et al.*, Phys. Rev. A **64**, 031405 (2001).
[3] S.Y.v.d. Meerakker, R.T. Jongma, H.L. Bethlem, and G. Meijer, Phys. Rev. A **64**, 041401(R) (2001).
[4] E.E. Nikitin and S.Y. Umanskii, *Theory of Slow Atomic Collisions* (Springer-Verlag, Berlin, 1984).
[5] Majorana, Nuovo Cimento **9**, 43 (1932).
[6] L.D. Landau and E.M. Lifshitz, *Quantum Mechanics* (Pergamon, Oxford, 1977).
[7] Cf. J. Vanier and C. Audoin, *The Quantum Physics of Atomic Frequency Standards* (Adam Hilger, Bristol, 1989), Vol. 1.
[8] K. Channapia, J. Pendlebury, and K. Smith, report, 1967 (unpublished).
[9] C.H. Townes and A.L. Schawlow, *Microwave Spectroscopy* (Dover, New York, 1975).
[10] H. Xu *et al.*, J. Chem. Phys. **103**, 5157 (1995).